Title:

On the Origin of Directional Variability in Earthquake Response Spectra: A Stochastic Covariance Framework

Authors:

Rajesh Rupakhety[1]

Víctor M. Hernández-Aguirre[2]

[1] Earthquake Engineering Research Centre, Faculty of Civil and Environmental Engineering, University of Iceland, Austurvegur 2a, 800 Selfoss, Iceland

Email: rajesh@hi.is

[2] Earthquake Engineering Research Centre, Faculty of Civil and Environmental Engineering, University of Iceland, Austurvegur 2a, 800 Selfoss, Iceland

Email: victorh@hi.is

Preprint Statement

This manuscript is a preprint and has not undergone peer review.

The manuscript is currently under review in Earthquake Engineering and Structural Dynamics.

This version is posted on EarthArXiv to ensure transparency, accessibility, and timely dissemination of the research.

The final published version, if accepted, may differ from this preprint.

Date of Preprint Posting:
22 March 2026

On the Origin of Directional Variability in Earthquake Response Spectra: A Stochastic Covariance Framework

Rajesh Rupakhety[1]*, Victor Moises Hernández-Aguirre[1]

Abstract

Directional variability of horizontal earthquake response spectra is commonly described using rotation-based measures such as RotD50 and RotD100, yet its physical and statistical origin remains unclear. This study shows that directional anisotropy arises fundamentally from finite-sample fluctuations of the covariance matrix of filtered ground-motion response. Even under perfectly isotropic excitation, covariance estimation over finite-duration records produces random polarization governed by Wishart statistics, establishing an intrinsic stochastic baseline for anisotropy. A geometric anisotropy measure, κ, is introduced based on the eigenvalue contrast of the response covariance matrix. It is shown that κ^2 follows an exact Beta distribution determined by the effective number of statistically independent realizations. Extension to oscillator response reveals that this effective number depends on oscillator bandwidth and energetic duration, leading to a closed-form scaling that explains the observed increase of anisotropy with period. A record-conditioned isotropic surrogate framework is developed to isolate this stochastic baseline in real ground motions while preserving spectral content and temporal envelope. Simulations and surrogate ensembles confirm that the Wishart-based model accurately captures the variability of directional anisotropy.The results show that rotation-based measures such as RotD100 and RotD50 do not directly quantify anisotropy, but combine covariance-driven geometric effects with stochastic peak selection. The proposed formulation provides a stochastic foundation for interpreting and modelling directional ground-motion fields in seismic hazard analysis.

.

Keywords: directionality, response spectra, peak factor, sample covariance, near-fault ground motions, polarization

1. Introduction

Directional variability of horizontal earthquake ground motion is typically summarized using rotation-invariant measures such as RotD50 and RotD100, defined as percentiles of the response obtained by rotating the two horizontal components through all non-redundant angles (Boore, 2010; Rupakhety and Sigbjörnsson, 2013). These measures provide stable scalar quantities for ground-motion prediction and seismic hazard

[1] Earthquake Engineering Research Center, Faculty of Civil and Environmental Engineering, University of Iceland, Austurvegur 2a, 800 Selfoss, Iceland
* Corresponding author

analysis, but they do not directly reveal the structure or origin of directional variability itself.

A large body of work has investigated empirical relationships between rotation-based ratios, particularly RotD100/RotD50, and conventional ground-motion predictors such as magnitude, distance, and site conditions (Boore and Kishida, 2017; Shahi and Baker, 2014; Watson-Lamprey and Boore, 2007). These studies have provided practical conversion relationships and adjustment factors that enable hazard models formulated for one horizontal-component definition to be applied to another. A consistent observation across datasets, however, is that directional ratios exhibit weak and often inconsistent scaling with traditional predictors. Although systematic trends with oscillator period and shaking duration have been reported (Poulos et al., 2021), much of the remaining variability appears difficult to attribute to identifiable source, path, or site parameters. This behaviour has led to the interpretation that directional variability is largely random or irreducible.

The absence of strong predictor scaling, however, does not imply absence of structure. Directional spectral response can be viewed not merely as a collection of rotated scalar values but as a continuous angular field defined over orientation. Recent developments have shown that this field admits a compact harmonic representation in which the squared directional spectrum is determined by the principal axes of response and a small number of scalar invariants (Rupakhety and Hernández-Aguirre, 2026a). Within this representation, the contrast between orthogonal principal responses is governed by a single anisotropy parameter, denoted here as κ_{psa}. All common rotation-based operators, including RotD50, RotD100, and related percentiles, can be expressed as functions of this parameter together with an overall amplitude scale. The parameter κ_{psa} therefore acts as a latent variable controlling directional amplification and the spread between rotation-invariant measures.

Although this representation clarifies the geometric structure of the directional field, the physical and stochastic origin of spectral anisotropy remains unclear. Examination of directional response across large ground-motion datasets reveals two persistent empirical features. First, anisotropy exhibits substantial variability that does not collapse under conventional predictors such as magnitude and distance. Second, its magnitude increases systematically with oscillator period. These observations suggest the presence of an intrinsic stochastic mechanism governing directional anisotropy that operates independently of specific physical regimes.

The present study proposes that this baseline arises from finite-sample covariance anisotropy of filtered ground motion. Even when the underlying excitation is perfectly isotropic, estimation of covariance from a finite time series produces random polarization of the response field. This phenomenon is formally described by Wishart statistics (Muirhead, 2009) for sample covariance matrices. When combined with the

bandwidth reduction imposed by linear single-degree-of-freedom (SDOF) filtering, the effective number of statistically independent realizations decreases with increasing oscillator period. The resulting reduction in effective degrees of freedom naturally produces larger expected anisotropy at long periods. Envelope non-stationarity further modulates this behaviour through the effective energetic duration of motion.

To isolate the Wishart mechanism, we introduce a geometric anisotropy measure κ_{rms} defined from the eigenvalues of the covariance matrix of pseudo-acceleration response. This quantity captures the purely geometric contrast between orthogonal principal responses and is independent of peak-selection effects. We show that the anisotropy parameter governing directional spectral amplitudes, κ_{psa}, can be expressed as a nonlinear transformation of κ_{rms} and a stochastic peak-factor anisotropy term. The resulting relationship takes a Möbius form that becomes additive in inverse hyperbolic tangent space, revealing a simple structural connection between covariance-driven anisotropy and peak-factor modulation.

The present work introduces a mechanistic framework that explains directional spectral anisotropy as an intrinsic consequence of finite-sample covariance statistics of filtered ground motion. The principal contributions are threefold. First, we separate directional variability into two distinct mechanisms: geometric anisotropy arising from covariance fluctuations and stochastic modulation associated with peak selection. Second, we show that the squared geometric anisotropy is a simple transformation of Wishart eigenvalue statistics and therefore follows an exact Beta distribution, providing the first closed-form stochastic model for directional anisotropy. Third, we connect the effective degrees of freedom governing this distribution to the bandwidth of SDOF-filtered response and to the energetic duration of ground motion. These results establish a stochastic baseline for directional spectral anisotropy that exists even in the absence of physical directional effects.

The objective of this paper is therefore to derive and validate the stochastic baseline for directional spectral anisotropy. We first formalize the directional field representation and introduce κ_{rms} and its relationship to κ_{psa}. We then derive the finite-sample covariance scaling implied by Wishart statistics and establish its dependence on effective degrees of freedom for filtered response. The influence of envelope non-stationarity is incorporated through an energetic duration measure. Finally, we demonstrate how peak-selection operators combine with geometric anisotropy to produce the observed curvature of rotation-based ratios. By separating intrinsic stochastic structure from physically induced polarization, the framework developed here provides a mechanistic foundation for interpreting directional ground-motion variability and establishes the basis for probabilistic modelling of spectral anisotropy.

2. Directional Response Field and Anisotropy Invariants

2.1 RMS covariance and geometric anisotropy

Let $\mathbf{a}(t) \in \mathbb{R}^2$ denote the two horizontal components of an oscillator's pseudo-acceleration response at a fixed period T. For a direction $\theta \in [0, \pi)$, the directional response is defined as

$$a(t, \theta) = \mathbf{u}(\theta)^\top \mathbf{a}(t), \mathbf{u}(\theta) = \begin{pmatrix} \cos\theta \\ \sin\theta \end{pmatrix}. \quad (1)$$

The response covariance matrix is

$$\mathbf{C} = \mathbb{E}\,[\mathbf{a}(t)\mathbf{a}(t)^\top],$$

and the directional second moment (variance) is

$\sigma_a^2(\theta) = \mathbb{E}[a(t,\theta)^2] = \mathbf{u}(\theta)^\top \mathbf{C}\mathbf{u}(\theta)$.

Let $\lambda_1 \geq \lambda_2 \geq 0$ denote the eigenvalues of $\mathbf{C}$, and let θ_0 be the eigenvector direction corresponding to λ_1. In this principal coordinate system the root mean squared (RMS) field is exactly elliptical,

$$\sigma_a^2(\theta) = \bar{\sigma}_a^2[1 + \kappa_{\mathrm{rms}} \cos 2(\theta - \theta_0)], \quad (2)$$

where

$$\bar{\sigma}_a^2 = \frac{\lambda_1+\lambda_2}{2}, \quad \kappa_{\mathrm{rms}} = \frac{\lambda_1-\lambda_2}{\lambda_1+\lambda_2}, 0 \leq \kappa_{\mathrm{rms}} < 1. \quad (3)$$

The parameter κ_{rms} therefore characterizes geometric polarization of the RMS response and depends solely on covariance structure. It is independent of peak factor selection and serves as the fundamental anisotropy variable in the present work.

2.2 Directional PSA and multiplicative structure

Directional pseudo-spectral acceleration is defined as

$$\mathrm{PSA}(\theta) = \max_t \; | \, a(t, \theta) \, |.$$

The directional peak factor is defined as

$$p(\theta) = \frac{\mathrm{PSA}(\theta)}{\sigma_a(\theta)}.$$

Consistent with the stochastic characterization established previously by Rupakhety and Hernández-Aguirre (2026b), we model the directional peak factor as

$$\ln \; p(\theta) = \mu_p + \varepsilon(\theta),$$

where $\varepsilon(\theta)$ is denoted as the stochastic peak-factor field. $\varepsilon(\theta)$ is π-periodic, has zero median over $[0, \pi)$, and is dominated by its first admissible harmonic with Rayleigh-distributed amplitude and approximately uniform phase. Defining the squared PSA field

$$S(\theta) = \mathrm{PSA}^2(\theta),$$

substitution yields

$$S(\theta) = \sigma_a^2(\theta)\exp(2\mu_p)\exp(2\varepsilon(\theta)).$$

Using the elliptical RMS form from (2) gives

$$S(\theta) = C[1 + \kappa_{\mathrm{rms}}\cos 2(\theta - \theta_0)]\exp(2\varepsilon(\theta)), \tag{4}$$

where $C = \bar{\sigma}_a^2 \exp(2\mu_p)$. This multiplicative representation defines a complete directional PSA field once κ_{rms}, the stochastic peak-factor field ε, and a scale constraint are specified.

2.3 Symmetric–antisymmetric decomposition and Möbius relation

Because $\varepsilon(\theta)$is π-periodic, it admits a natural decomposition with respect to a rotation by $\pi/2$:

$$\varepsilon^s(\theta) = \frac{\varepsilon(\theta) + \varepsilon(\theta + \pi/2)}{2}, \varepsilon^a(\theta) = \frac{\varepsilon(\theta) - \varepsilon(\theta + \pi/2)}{2}.$$

Then

$$\varepsilon(\theta) = \varepsilon^s(\theta) + \varepsilon^a(\theta), \varepsilon(\theta + \pi/2) = \varepsilon^s(\theta) - \varepsilon^a(\theta).$$

The symmetric component ε^s is preserved under a $\pi/2$ rotation and therefore modulates the overall scale of the field. The antisymmetric component ε^a changes sign and controls directional contrast. Evaluating the squared field in the RMS principal frame ($\theta_0 = 0$) at the orthogonal pair $\theta = (0, \pi/2)$ yields

$$S(0) = C(1 + \kappa_{\mathrm{rms}})\exp\big(2(\varepsilon^s + \varepsilon^a)\big),$$
$$S(\pi/2) = C(1 - \kappa_{\mathrm{rms}})\exp(2(\varepsilon^s - \varepsilon^a)).$$

Then, the PSA anisotropy invariant on this pair is defined as

$$\kappa_{\mathrm{psa}} = \frac{S(0) - S(\pi/2)}{S(0) + S(\pi/2)}.$$

After cancellation of the symmetric component, one obtains

$$\kappa_{\mathrm{psa}} = \frac{\kappa_{\mathrm{rms}} + \tanh(2\varepsilon^a)}{1 + \kappa_{\mathrm{rms}}\tanh(2\varepsilon^a)}. \tag{5}$$

Thus κ_{psa} is a Möbius transform of κ_{rms} driven solely by the antisymmetric peak-factor component. The symmetric component influences only the overall level and does not affect anisotropy.

2.4 Scale anchoring via PSA invariants

The PSA invariant associated with the RMS principal orthogonal pair is defined as

$$I_1 = S(0) + S(\pi/2).$$

Substitution gives

$$I_1 = C\big[(1 + \kappa_{\mathrm{rms}})e^{2\varepsilon(0)} + (1 - \kappa_{\mathrm{rms}})e^{2\varepsilon(\pi/2)}\big].$$

Hence the scale factor is

$$C = \frac{I_1}{(1+\kappa_{\mathrm{rms}})e^{2\varepsilon(0)} + (1-\kappa_{\mathrm{rms}})e^{2\varepsilon(\pi/2)}}. \tag{6}$$

Because I_1 is defined from squared PSA values, it already embeds two realizations of the peak-factor field. Conditioning on I_1 therefore fixes the overall level without requiring separate knowledge of the RMS scale or the median peak factor. Empirically, I_1 is closely

related to RotD50[2] under dominant first-harmonic structure, providing a practical anchoring quantity.

2.5 Implications for anisotropy modelling

Previous work (Rupakhety and Hernández-Aguirre, 2026a) derived accurate closed-form approximations for rotation-invariant operators by projecting the directional field onto its first harmonic. That approach provides compact operator relations but does not uniquely determine the underlying field and requires additional empirical calibration for quadrature contributions.

The multiplicative representation introduced here defines the full directional field without empirical constants. Quadrature structure arises naturally from the stochastic peak-factor field ε. Within this framework, κ_{rms} emerges as the fundamental anisotropy variable: it reflects covariance geometry alone and is unaffected by peak selection. In contrast, κ_{psa} incorporates two realizations of the peak-factor field and is therefore intrinsically noisier. Since the complete PSA field is recoverable from κ_{rms} and ε, modelling κ_{rms} provides a cleaner and more mechanistic basis for describing directional anisotropy. Closed-form operator relations can be obtained subsequently through the Möbius mapping (Eq. 5) and the statistical properties of ε.

3. Wishart Baseline for Geometric Anisotropy

3.1 Finite-sample covariance of isotropic Gaussian response

To identify the intrinsic stochastic component of directional anisotropy, consider an idealized two-component pseudo-acceleration response process at a fixed oscillator period,

$$\mathbf{X}(t) = \begin{bmatrix} X_1(t) \\ X_2(t) \end{bmatrix},$$

assumed to be zero-mean, stationary, Gaussian, and second-order isotropic. Isotropy implies that the population covariance matrix is proportional to the identity,

$$\mathbb{E}[\mathbf{X}(t)\mathbf{X}^{\top}(t)] = \sigma^2 \mathbf{I}_2,$$

so that no preferred direction exists in the underlying response field. In practice, covariance is estimated from a finite record of duration D. If the process yields N statistically independent realizations, the sample covariance matrix is

$$\hat{\mathbf{C}} = \frac{1}{N}\sum_{i=1}^{N} \mathbf{X}_i \, \mathbf{X}_i^{\top}.$$

Under the Gaussian assumption, the scaled matrix $N\hat{\mathbf{C}}$ follows a two-dimensional Wishart distribution (Muirhead, 2009; Wishart, 1928),

$$N\hat{\mathbf{C}} \sim \mathcal{W}_2(N, \sigma^2 \mathbf{I}_2).$$

Although the true covariance is isotropic, the sample covariance is random. Finite-sample fluctuations therefore induce apparent polarization even when the underlying excitation is perfectly isotropic.

3.2 Exact distribution of geometric anisotropy

Let $\lambda_1 \geq \lambda_2 > 0$ denote the eigenvalues of the sample covariance matrix $\hat{\mathbf{C}}$. For the isotropic 2×2 Wishart case, the distribution of κ_{rms} admits a particularly simple closed form. Let the trace and eigenvalue contrast be defined as

$$s = \lambda_1 + \lambda_2, d = \lambda_1 - \lambda_2.$$

The anisotropy variable is then

$$\kappa_{\mathrm{rms}} = \frac{d}{s}.$$

Equivalently, the eigenvalues may be written in terms of $(s, \kappa_{\mathrm{rms}})$ as

$$\lambda_1 = \frac{s}{2}(1 + \kappa_{\mathrm{rms}}),\ \lambda_2 = \frac{s}{2}(1 - \kappa_{\mathrm{rms}}).$$

This transformation from eigenvalues to trace–anisotropy coordinates separates the overall energy level of the covariance estimate (through s) from its geometric polarization (through κ_{rms}). For the isotropic Wishart distribution, the resulting joint density in these variables factorizes in a manner that allows the trace variable to be integrated out. Carrying out this change of variables and marginalization (Appendix A.1) yields the exact distribution

$$\kappa_{\mathrm{rms}}^2 \sim \mathrm{Beta}\left(1, \frac{N-1}{2}\right). \tag{7}$$

Thus, even under perfectly isotropic Gaussian excitation, the geometric anisotropy is a bounded random variable governed solely by the effective number of independent realizations N. In other words, directional polarization arises as an intrinsic finite-sample effect of covariance estimation even when there is no physical asymmetry in the excitation. From this distribution, exact moment expressions follow immediately (Appendix A.2). In particular,

$$\mathbb{E}[\kappa_{\mathrm{rms}}^2] = \frac{2}{N+1}.$$

Higher moments and closed-form expressions for the mean of κ_{rms} may likewise be obtained using Gamma function identities. These results establish a simple statistical baseline for directional anisotropy.

3.3 Large-N Scaling of Mean and Variance

For large N, Stirling's approximation for Gamma functions (Abramowitz and Stegun, 2006) yields simple asymptotic expressions (Appendix A.3):

$$\mathbb{E}[\kappa_{\mathrm{rms}}] \approx \sqrt{\frac{\pi}{2N}},$$

$$\mathrm{Var}(\kappa_{\mathrm{rms}}) \approx \frac{4-\pi}{2N}.$$

These expressions quantify the intrinsic stochastic baseline imposed by finite-sample covariance fluctuations. Any observed anisotropy must therefore be interpreted relative to this baseline before attributing directional structure to physical mechanisms.

3.4 Interpretation as random polarization

The statistical result derived above admits a simple geometric interpretation. The population covariance matrix is circular and possesses no distinguished axis. The sample covariance matrix, however, is a random perturbation of this isotropic state. Its principal eigenvector therefore identifies a randomly oriented direction in the plane, and the corresponding eigenvalue contrast quantifies the magnitude of finite-sample fluctuation.

In two dimensions, the principal direction is uniformly distributed over $[0, \pi)$, while the anisotropy magnitude depends only on the effective number of degrees of freedom N. The emergence of directional structure under isotropic excitation is therefore not paradoxical; it is an inevitable consequence of finite-sample covariance estimation. The baseline magnitude of anisotropy is controlled entirely by the scaling $N^{-1/2}$.

4. SDOF Filtering and Effective Degrees of Freedom

4.1 Effective degrees of freedom for covariance estimation

Section 3 showed that geometric anisotropy under isotropic Gaussian excitation is governed by a Wishart baseline parameterized by the number of statistically independent realizations (N). For continuous response time series, this number must be replaced by an effective number of degrees of freedom, N_{eff}, appropriate to the covariance estimator.

Importantly, N_{eff} for covariance estimation is not determined simply by the number of sampled points, nor by zero-crossing rates or cycle counts. Because anisotropy is defined through eigenvalues of the sample covariance matrix, the relevant object is the variance of a quadratic functional.

Let $X(t)$ and $Y(t)$ be independent, zero-mean, stationary Gaussian processes with identical variance σ^2 and common normalized autocorrelation function $\rho(\tau)$, with $\rho(0) = 1$. Then, the continuous-time sample cross-covariance estimator over the duration D is

$$\hat{C}_{XY} = \frac{1}{D}\int_0^D X(t)Y(t)\, dt,$$

For correlated Gaussian processes, when D is large relative to the correlation decay scale, fourth-moment factorization (Appendix A.4) yields

$$\mathrm{Var}\left(\hat{C}_{XY}\right) \approx \frac{\sigma^4}{D}\, 2\int_0^\infty \rho^2(\tau)\; d\tau.$$

Matching this variance to the independent-sample (Wishart) variance form defines the effective degrees of freedom for covariance estimation as

$$N_{\text{eff}} \approx \frac{D}{2\int_0^\infty \rho^2(\tau)\; d\tau}.$$

Thus, for geometric anisotropy under isotropic Gaussian excitation, the controlling parameter is the integral of the squared autocorrelation function. Period dependence of anisotropy therefore enters naturally through the response autocorrelation structure.

4.2 Narrowband autocorrelation of SDOF response

Consider the pseudo-acceleration response of a linear SDOF oscillator with natural frequency $\omega_n = 2\pi/T$ and damping ratio ξ subjected to broadband Gaussian excitation. For lightly damped response, the process is narrowband around ω_n and the normalized autocorrelation is well approximated by the standard exponentially decaying sinusoid

$$\rho(\tau) \approx e^{-\alpha|\tau|}\cos(\omega_d\tau), \alpha = \xi\omega_n, \omega_d \approx \omega_n\sqrt{1-\xi^2}.$$

Substituting into the covariance-based definition of N_{eff} requires $\int_0^\infty \rho^2(\tau)\, d\tau$. Using $\cos^2(\omega_d\tau) = \frac{1}{2}[1+\cos(2\omega_d\tau)]$, one finds that for $\omega_d \gg \alpha$ (light damping) the oscillatory term contributes only a small correction, and the leading-order term is

$$\int_0^\infty \rho^2(\tau)\, d\tau \approx \frac{1}{4\alpha}.$$

Therefore,

$$N_{\text{eff}} \approx \frac{D}{2(1/(4\alpha))} = 2\alpha D = 2\xi\omega_n D = \frac{4\pi\xi D}{T}. \quad (8)$$

4.3 Period scaling of geometric anisotropy

Substituting the SDOF expression for effective degrees of freedom, into the large-N_{eff} asymptotic form of the Wishart baseline yields an explicit period dependence for geometric anisotropy. In particular, using the asymptotic mean expression gives

$$\mathbb{E}[\kappa_{\text{rms}}(T)] \approx \sqrt{\frac{T}{8\,\xi D}}. \quad (9)$$

The square-root period scaling arises directly from the collapse of effective bandwidth under SDOF filtering, which reduces the number of statistically independent covariance realizations as period increases.

4.4 Numerical verification

The analytical scaling derived above was verified by Monte Carlo simulation of isotropic Gaussian excitation filtered through linear SDOF oscillators. For each oscillator period T, independent two-component realizations were generated, the pseudo-acceleration response computed, and the sample covariance matrix evaluated from the resulting time series. The geometric anisotropy $\kappa_{\text{rms}}(T)$ was obtained from the eigenvalues of the sample covariance. Ensemble estimates of the mean and standard deviation are compared with the theoretical predictions based on the covariance-estimator effective degrees of freedom $N_{\text{eff}} \approx 4\pi\xi D/T$. The results of the simulations, shown in the left panel of Figure 1, confirm the predicted $\sqrt{T}$ dependence, which appears as an approximately linear trend in log–log representation, as well as the associated increase in variability with period.

The right panel in Figure 1 shows the corresponding distribution of RotD100/RotD50 ratios obtained from directional peak response. The ratios exhibit a mild curvature with

period rather than the power-law form observed for κ_{rms}, reflecting the additional influence of the peak-selection operator. The width of the RotD100/RotD50 confidence band increases with period, consistent with the increasing dispersion of κ_{rms} under decreasing effective degrees of freedom. At short periods, where κ_{rms} becomes small, the RotD ratio decreases only gradually, indicating that stochastic peak-factor modulation remains operative even when covariance anisotropy is weak. Overall, these results demonstrate that the finite-sample covariance mechanism governs the baseline magnitude and dispersion of directional response, whereas peak selection mainly modifies its period dependence, giving rise to the curvature observed in the RotD100/RotD50 ratios.

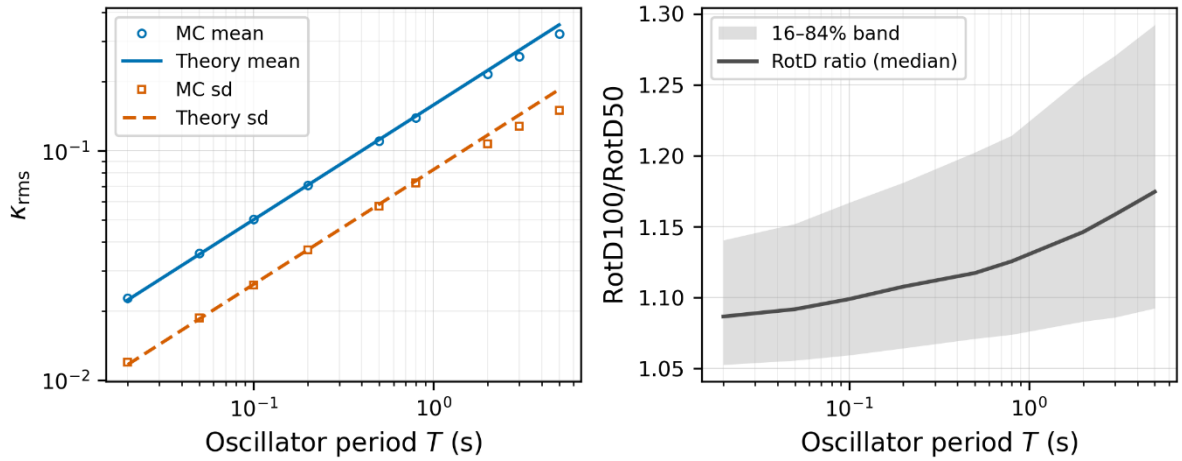

Figure 1. Monte Carlo verification of the SDOF-filtering baseline. Left: ensemble mean and standard deviation of $\kappa_{rms}(T)$ compared with the theoretical scaling based on $N_{eff} \approx 4\pi\xi D/T$. Right: ensemble median and 16–84% quantile band of RotD100/RotD50 computed from 1° rotations of pseudo-acceleration response. 5000 simulations were run, each with a duration of 100s. Damping ratio is fixed at 5% of critical.

5. Envelope modulation and energetic duration

5.1 Amplitude-modulated excitation

The development in Section 4 assumed stationary Gaussian excitation over a finite observation window of duration D. Real earthquake ground motions are strongly non-stationary: energy is concentrated within a finite time interval and modulated by an evolving amplitude envelope. To incorporate this effect without altering the stochastic covariance mechanism identified previously, we write the horizontal excitation components as

$$g_i(t) = w(t)\, u_i(t), i = 1,2,$$

where $u_i(t)$ are zero-mean, stationary, isotropic Gaussian processes and $w(t)$ is a deterministic envelope describing temporal modulation of excitation amplitude. The envelope is assumed to vary slowly relative to the correlation time imposed by SDOF filtering. Because the SDOF system is linear, response non-stationarity arises from the excitation envelope rather than from modification of the underlying stochastic structure.

Under this representation, the finite-sample covariance mechanism derived in Sections 3 and 4 remains unchanged. The Wishart structure of anisotropy therefore persists; only

the effective temporal support contributing to covariance estimation is altered by the envelope.

5.2 Energetic effective duration

The variance of quadratic estimators such as covariance depends on fourth-order time integrals of the process. Under the slowly varying envelope approximation (Appendix A.6), variance matching leads to a natural definition of an energetic effective duration,

$$D_{\text{eff}}^{(g)} = \frac{\left(\int w^2(t)\,dt\right)^2}{\int w^4(t)\,dt}. \tag{10}$$

This quantity measures the effective temporal support of squared amplitude. It is analogous to the effective support measures that arise in variance calculations for quadratic estimators of non-stationary random processes. It equals the total duration D when the envelope is constant and decreases as energy becomes more concentrated in time. In contrast to commonly used duration measures such as significant duration based on Arias intensity, this definition arises directly from variance matching of the covariance estimator and is therefore the appropriate support measure governing geometric anisotropy. Importantly, $D_{\text{eff}}^{(g)}$ depends only on excitation non-stationarity and is independent of oscillator properties. Substituting this duration into the effective degrees-of-freedom expression derived in Appendix A yields

$$N_{eff}(T) \approx \frac{4\pi\xi D_{eff}^{(g)}}{T}.$$

Envelope modulation therefore enters anisotropy scaling exclusively through reduction of effective duration.

5.3 Period scaling under non-stationarity

Replacing D by $D_{\text{eff}}^{(g)}$ in the large-N_{eff} asymptotic Wishart expressions gives

$$\mathbb{E}[\kappa_{\text{rms}}(T)] \approx \sqrt{\frac{T}{8\,\xi\,D_{\text{eff}}^{(g)}}}, \tag{11}$$

$$\text{sd}(\kappa_{\text{rms}}(T)) \approx \sqrt{\frac{4-\pi}{8\pi\,\xi\,D_{\text{eff}}^{(g)}}}\,\sqrt{T}. \tag{12}$$

Thus, geometric anisotropy increases with oscillator period as $\sqrt{T}$, while decreasing with both damping and energetic duration. Concentration of energy in time reduces effective degrees of freedom and correspondingly increases both the expected magnitude and the variability of anisotropy. Envelope non-stationarity does not alter the stochastic Wishart mechanism itself; it rescales the degrees of freedom that govern the distribution of anisotropy.

5.4 Numerical verification

Monte Carlo simulations were performed to verify the envelope-modified scaling derived above. A smooth Gaussian envelope centred at mid-record (standard deviation equal to 0.15 D) and filtered through linear SDOF oscillators with damping ratio ξ=5%. A total of 5000 independent realizations were generated using a simulation window length of D=100 s with time step dt=0.005 s.

Figure 2 (left panel) compares the ensemble mean and standard deviation of $\kappa_{\mathrm{rms}}(T)$ with the theoretical prediction obtained by substituting the energetic effective duration $D_{\mathrm{eff}}^{(g)}$ into the effective degrees-of-freedom expression derived in Section 4. The solid curves show excellent agreement across most of the period range. In contrast, dashed curves obtained by substituting the total window duration D systematically underpredict anisotropy, demonstrating that non-stationarity reduces the effective support of excitation, thus increasing the geometric anisotropy. Minor deviations at the longest periods arise as the SDOF correlation time becomes comparable to the envelope width, weakening the slowly varying envelope approximation underlying the derivation.

The right panel in Figure 2 shows the corresponding distribution of RotD100/RotD50 ratios. As in Section 4, the median ratio exhibits mild curvature with period, reflecting the additional influence of the peak-selection operator. Moreover, both, the median ratios and the width of the confidence band are larger than those shown in Figure 1, in accordance with the introduction of $D_{\mathrm{eff}}^{(g)}$ in (11) and (12). Furthermore, the 16–84% band in the right panel indicates that RotD100/RotD50 ratios approaching 1.35 may occur at long periods even under perfectly isotropic excitation.

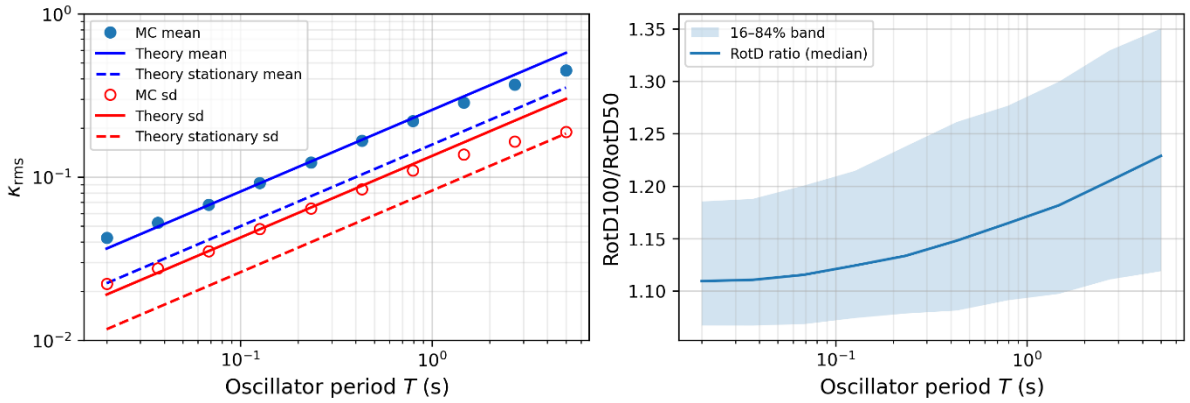

Figure 2. Monte Carlo verification of envelope-modified anisotropy. Left: ensemble mean and standard deviation of $\kappa_{rms}(T)$ from 5000 simulations of enveloped isotropic Gaussian excitation (total duration $D = 100$s, $dt = 0.005$s, $\xi = 5\%$), compared with theoretical predictions using the energetic effective duration $D_{eff}^{(g)}$(solid lines) and the full window length D(dashed lines). Right: median and 16–84% band of RotD100/RotD50 ratios obtained from the same simulations.

5.5 Verification of the Wishart–Beta model for κ_{rms}^2

In Figures 1 to 3, the mean and standard deviation of κ_{rms} from different excitation models were compared with the theoretical predictions of the Wishart-based Beta distribution. Figure 3 complements those results by examining the full distribution of κ_{rms}^2 across progressively more realistic excitation models. Panel (a) shows the idealized case of independent Gaussian samples, for which the covariance matrix follows the classical Wishart distribution exactly; accordingly, the empirical distribution of κ_{rms}^2 matches the predicted Beta law closely. Panel (b) considers stationary Gaussian excitation filtered through a linear SDOF oscillator. Although filtering introduces strong temporal correlation and reduces the number of effectively independent samples, the Beta model remains accurate when parameterized by the theoretical effective degrees of freedom N_{eff}. Panel (c) further includes non-stationary excitation through a slowly varying

amplitude envelope. In this case, temporal modulation of signal energy also influences the covariance estimator, so that the effective sample size is governed by the energetic duration of the response. Even under this additional non-stationarity, the empirical distribution of κ_{rms}^2 remains well captured by the same Beta model.

Figure 3 also includes independently fitted Kumaraswamy (1980) distributions. The Kumaraswamy family provides a flexible bounded distribution on the unit interval and reproduces the empirical distributions closely across all cases. Owing to its analytical simplicity and parametric flexibility, it provides a convenient surrogate representation of the empirical distribution of κ_{rms}^2.

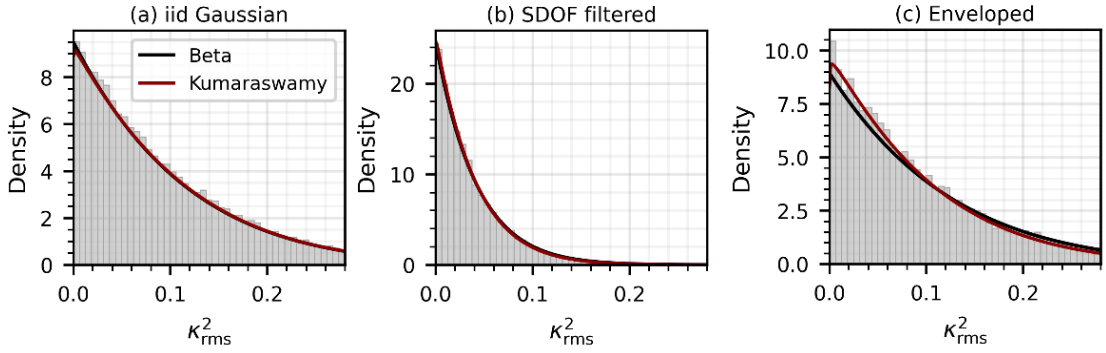

Figure 3. Empirical distributions of κ_{rms}^2 for three excitation models: (a) independent Gaussian samples, (b) stationary SDOF-filtered Gaussian response, and (c) SDOF-filtered enveloped Gaussian excitation. Gray histograms show simulated ensembles. Black curves denote the Wishart-derived Beta model, while red curves show independently fitted Kumaraswamy distributions. SDOF period is 0.5s and damping ratio is 5%.

6. Record-conditioned isotropic surrogates

The developments in Sections 3–5 established that geometric anisotropy arises intrinsically from finite-sample covariance fluctuations of filtered Gaussian processes. Real earthquake ground motions, however, differ from this idealization in several important respects. They are non-Gaussian, non-stationary, and may exhibit persistent directional structure associated with source radiation pattern (Kotha et al., 2019), directivity effects (Bradley and Baker, 2015), path heterogeneity (e.g., Campbell, 1991; Pischiutta et al., 2012), and local site-response effects (Burjánek et al., 2014; Vidale et al., 1991). Consequently, direct comparison of real-record anisotropy with the closed-form Wishart expressions derived previously would conflate intrinsic stochastic variability with physical polarization mechanisms.

To isolate the stochastic baseline within real data, we construct record-conditioned isotropic surrogates. These surrogates preserve the temporal envelope and the combined horizontal power spectrum of a given record while enforcing isotropy in ensemble expectation. In this way, the effective duration, bandwidth, and oscillator filtering characteristics of the real motion are retained, but any persistent directional covariance structure is removed. Comparison of the real record with its surrogate ensemble therefore permits a direct assessment of whether the observed anisotropy can be explained by finite-sample covariance statistics alone, or whether additional physical mechanisms are required.

6.1 Surrogate construction

Considering a recorded horizontal acceleration pair $U(t), V(t)$, the instantaneous horizontal amplitude is defined as

$$A(t) = \sqrt{U^2(t) + V^2(t)}.$$

To characterize excitation non-stationarity, we extract a smooth envelope function $w(t)$ representing the slowly varying amplitude modulation of the record. The envelope is obtained by smoothing $A(t)$ over a time scale large relative to the dominant oscillation periods but small relative to the overall duration. This procedure retains the energetic support of the motion while filtering high-frequency carrier fluctuations. Next, we compute the combined horizontal power spectrum

$$S_H(f) = S_{UU}(f) + S_{VV}(f),$$

where S_{UU} and S_{VV} denote the individual component spectra. This spectrum defines the total horizontal energy content independent of orientation. We then generate two independent, zero-mean, stationary Gaussian carrier processes $u_1(t)$ and $u_2(t)$such that

$$S_{u_1u_1}(f) = S_{u_2u_2}(f) = \frac{1}{2} S_H(f), S_{u_1u_2}(f) = 0.$$

By construction, the ensemble covariance of the carrier pair is isotropic. Each surrogate realization is formed through amplitude modulation,

$$g_i(t) = w(t)\, u_i(t), i = 1,2.$$

Because the SDOF system is linear, this procedure preserves the envelope-induced non-stationarity and the oscillator-filtered bandwidth characteristics of the original record. However, any persistent cross-component covariance or preferred polarization present in the real motion is eliminated in ensemble expectation. The surrogate ensemble therefore defines a null model representing isotropic excitation with identical duration, envelope, and spectral content of the original record.

6.2 Demonstration on a Representative Record

To illustrate the proposed mechanism at the record level, we consider station 6305 (TK network) from the 6 February 2023 Kahramanmaraş earthquake (M_w 7.7, R_{JB} = 103.7 km; Lanzano et al., 2021). The record exhibits moderate duration and amplitude without pronounced directional polarization in the raw accelerograms, making it suitable as a representative example. Using the procedure outlined above, we generate 500isotropic surrogate realizations that preserve the record's combined horizontal spectrum and its non-stationary envelope while enforcing ensemble isotropy.

Figure 4 summarizes the results. Panel (a) confirms preservation of the combined horizontal power spectral density. Panel (b) shows that the geometric anisotropy measure $\kappa_{\mathrm{rms}}(T)$ of the real record lies within the stochastic band generated by the surrogates, and that its mean growth with period is captured by the theoretical prediction based on the energetic effective duration $D_{\mathrm{eff}}^{(g)}$ (eq. 11), which implies that for this specific record, the anisotropy is mainly due the finite-sample covariance mechanism, and is present even in the absence of physical directional effects. Panel (c) demonstrates analogous behaviour for the RotD100/RotD50 ratio. Notably, at some periods the record

approaches the theoretical elliptical limit of $\sqrt{2}$ in the rotation-based ratio, demonstrating that individual ground motions can exhibit large apparent directional effects purely due to finite-sample variability in κ_{rms}, further amplified by peak selection. Finally, Panel (d) illustrates the sensitivity of the theoretical scaling to the choice of duration definition. Using the full window duration systematically underestimates anisotropy. However, the significant duration $D_{5\text{–}95}$ provides a similar scaling to $D_{\mathrm{eff}}^{(g)}$.

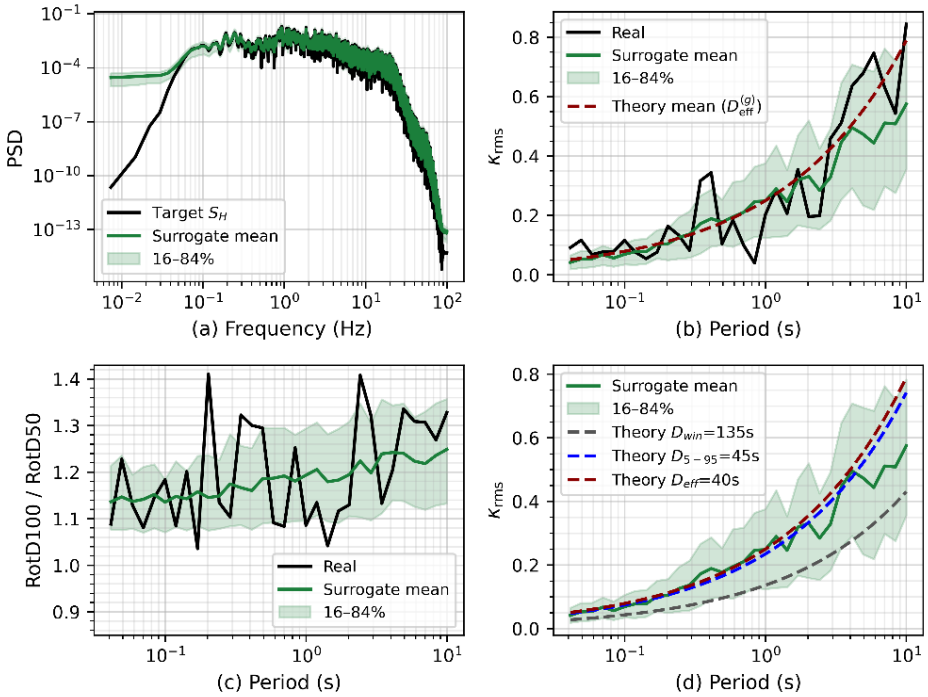

Figure 4. Record-conditioned isotropic surrogate validation for station 6305 (TK), 6 Feb 2023 Kahramanmaraşearthquake (M_w 7.7, R_{JB} 103.7 km): (a) spectrum preservation, (b) $\kappa_{rms}(T)$ for record, surrogates, and energetic-duration theory, (c) RotD100/RotD50, (d) duration sensitivity.

Extending the results of Figure 3, Figure 5 shows that the Wishart–Beta model also captures the distribution of κ_{rms}^2 in the record-conditioned isotropic surrogate ensemble. Despite the more realistic constraints in the surrogates, the empirical distribution remains in close agreement with the predicted Beta law. The independently fitted Kumaraswamy distribution provides a similarly accurate approximation and offers a convenient practical representation of the stochastic baseline distribution.

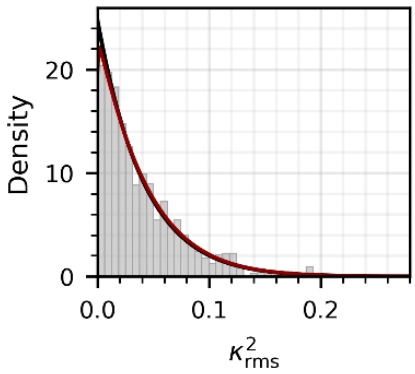

Figure 5. Empirical distribution of κ^2_{rms} from the isotropic surrogates conditioned on record from station 6305 (TK), 6 Feb 2023 Kahramanmaraş earthquake (M_w 7.7, R_{JB} 103.7 km). Gray histograms show simulated ensembles. The black curve denotes the Wishart-derived Beta model, while the red curve shows the fitted Kumaraswamy distribution.

6.3 Pulse-Like Record: Physical Perturbation of the Wishart Baseline

To illustrate how physically induced directional structure manifests relative to the stochastic baseline derived in Sections 3–5, we consider a pulse-like ground motion selected from the database (station BAR, 1979 M_w 6.9 Montenegro earthquake). Pulse-like motions (see for example, Rupakhety et al., 2011) provide a well-understood and widely accepted physical mechanism for directional amplification associated with rupture directivity. They therefore serve as an appropriate test case for examining how coherent physical polarization interacts with finite-sample covariance variability.

Figure 6 summarizes the comparison between the real record and its surrogate ensemble. The left panel shows the geometric anisotropy measure $\kappa_{rms}(T)$ for the real record, together with the surrogate ensemble mean and its 16–84% band. Also shown are two theoretical mean baseline curves: the asymptotic duration-based scaling and the non-asymptotic mean obtained from the exact Wishart–Beta distribution using the effective degrees of freedom $N_{\mathrm{eff}}(T)$. The $\kappa_{rms}(T)$ for the real record lies persistently above the surrogate mean and frequently near the upper edge of the central surrogate band across a broad period range. Because the surrogates preserve duration and spectral content, this systematic elevation cannot be attributed to finite-sample covariance variability alone. Instead, it indicates record-specific directional polarization superimposed on the Wishart baseline. In other words, the record exhibits a genuine physical anisotropy component that survives removal of stochastic covariance fluctuations. The record shows additional amplification of $\kappa_{rms}(T)$ in the vicinity of the pulse period T_p, consistent with the expected effect of directivity-induced energy concentration at that scale. Importantly, the pulse effect appears as a localized perturbation on top of a broadband polarization offset, rather than as an isolated narrow-band phenomenon.

The theoretical curves deviate from the surrogate ensemble at long periods. The asymptotic duration-based expression increasingly overpredicts anisotropy as T grows, reflecting breakdown of the large-N_{eff} assumption. The non-asymptotic mean derived from the exact Wishart–Beta formulation reduces this discrepancy but does not eliminate it entirely. This residual mismatch is attributable not to failure of the Wishart mechanism itself, but to approximations used in deriving $N_{\mathrm{eff}}(T)$, including the narrowband autocorrelation model and the slowly varying envelope assumption. For

pulse-like motions, the energetic duration D_{eff} is small, leading to small N_{eff} and increased sensitivity to these approximations.

The right panel of Figure 6 shows the corresponding RotD100/RotD50 ratio. In contrast to $\kappa_{rms}(T)$, the rotation-based ratio exhibits substantially larger variability, with pronounced intermittent peaks. The surrogate band is wide across nearly the entire period range, including short periods. This behavior differs from non-pulse example examined previously, where the surrogate band was narrow at short periods and widened progressively with increasing T. The explanation lies in the effective duration. Pulse-like motions typically concentrate energy into a relatively short time interval, reducing D_{eff} and therefore $N_{\text{eff}}(T)$ at all periods. As established in Sections 4 and 5, smaller N_{eff} directly increases baseline anisotropy variance. Thus, even under isotropic excitation with identical envelope and spectrum, substantial scatter in rotation-based ratios is expected. The wide surrogate band therefore reflects the structural stochastic variability imposed by limited effective duration.

The real record exhibits pronounced peaks in RotD100/RotD50 near the pulse period, in some instances approaching the theoretical upper bound associated with completely polarized response. Additional elevated peaks are observed at shorter periods, consistent with the broadband polarization visible in $\kappa_{rms}(T)$. At very short periods, the real ratio may fall below the surrogate median. This behavior is not paradoxical: when $\kappa_{rms}(T)$ is modest, the rotation-based ratio becomes strongly influenced by realization-to-realization variability in the peak-selection operator. A single record can therefore lie anywhere within the wide surrogate band without contradicting the presence of underlying polarization.

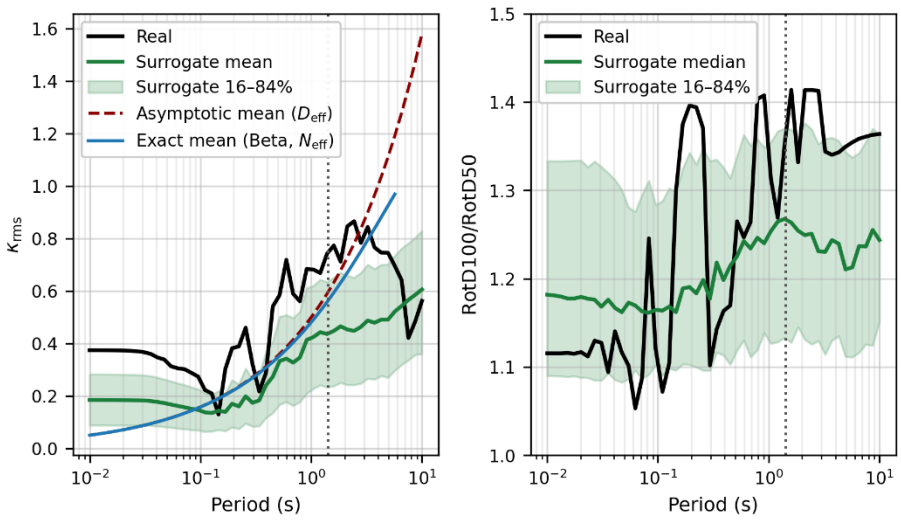

Figure 6. Pulse-like record from the 15 April 1979 Montenegro earthquake (event ID ME-1979-0003, M_w 6.9), recorded at station BAR (R_{JB} ≈ 3 km). Left: $\kappa_{rms}(T)$ for the real record (black) compared with record-conditioned isotropic surrogate ensemble (green mean and 16–84% band), with asymptotic (red dashed) and exact Wishart–Beta (blue) baseline predictions; vertical line marks the pulse period T_p. Right: corresponding RotD100/RotD50 ratio with surrogate median and band. The record shows systematic polarization relative to the stochastic baseline, with elevated anisotropy near T_p and substantial variability due to limited effective duration.

A central insight emerges from this example. Pulse-like ground motions introduce coherent directional structure, producing systematic upward shifts in κ_{rms} relative to the isotropic baseline. However, such records often possess short energetic duration,

resulting in reduced effective degrees of freedom and correspondingly elevated stochastic variability. Physical polarization therefore manifests primarily as a regime-dependent mean shift superimposed on a substantial Wishart-driven baseline variance.

Near-fault pulse-like motions often contain only a small number of effective oscillatory cycles. In this regime the covariance estimator of the response process becomes poorly conditioned, and the inferred orientation of directional amplification can vary substantially due to finite-sample fluctuations. This may help explain why pulses are frequently observed in multiple orientations, even when rupture directivity and source-radiation pattern would suggest a preferred direction.

These observation resolves an apparent contradiction. One might intuitively expect that strongly polarized motions would yield more predictable rotation-based ratios. In fact, the opposite can occur: physically intense but temporally compact motions can exhibit large mean anisotropy while retaining large sampling variability due to limited effective duration. The variance is governed by the Wishart mechanism and does not diminish simply because the population covariance departs from isotropy.

6.4 Illustrative example of site-controlled anisotropy: station ASS

Real ground-motion fields may also deviate from isotropic baseline when local site-response effects introduce preferred horizontal directions. To illustrate how such mechanisms appear in the κ_{rms} statistics, we examine recordings from station ASS of the Italian Strong Motion Network.

Station ASS is located in Assisi, central Italy (43.075°N, 12.604°E). The station is installed on the Assisi ridge above the Chiascio valley. According to the ESM metadata (Lanzano et al., 2021), the site has a shear-wave velocity V_{S30} of approximately 1050–1060 m/s, corresponding to rock conditions. However, the station is classified topographically as a ridge (classes T3–T4) with a slope of about 19°. Ridge and slope topography may produce directional amplification through wave scattering and focusing along the crest direction. Geological mapping indicates that the station is situated on carbonate formations of the Scaglia sequence that form the prominent Assisi ridge.

A total of 21 strong-motion recordings are available for this station in the dataset analysed here. Independent information on the site response is provided by ambient vibration measurements. Figure 7a shows the horizontal-to-vertical spectral ratio (HVSR) curve derived from microtremor recordings at the site, available from the ESM database. The HVSR exhibits a pronounced peak near approximately 3.4 Hz, indicating a resonance associated with the local site structure.

Figure 7b shows the station-averaged anisotropy measure κ_{rms} computed from the 21 strong-motion recordings. The black curve represents the mean across records, while the grey band denotes the 16–84% range. For comparison, the green curve shows the isotropic surrogate baseline obtained from record-conditioned stochastic simulations in which the horizontal components are rendered isotropic while preserving the observed spectra and envelopes.

Across a broad range of short oscillator periods, the observed κ_{rms} systematically exceeds the isotropic baseline. This indicates persistent directional amplification in the recorded motions that cannot be explained by stochastic fluctuations alone. The period range where this excess is most pronounced corresponds closely to the frequency band associated with the HVSR peak.

The agreement between the HVSR resonance and the elevated κ_{rms} values suggests that the anisotropy originates from site-controlled amplification. In this case, the ridge topography and local geological structure appear to favour amplification along certain horizontal directions, producing coherent directional structure in the ground-motion field. This directional site response manifests in the κ_{rms} statistics as a systematic shift above the isotropic Wishart baseline. Although this example is intended primarily as an illustration, it demonstrates how physically meaningful directional effects can be identified through deviations of κ_{rms} from the isotropic stochastic baseline.

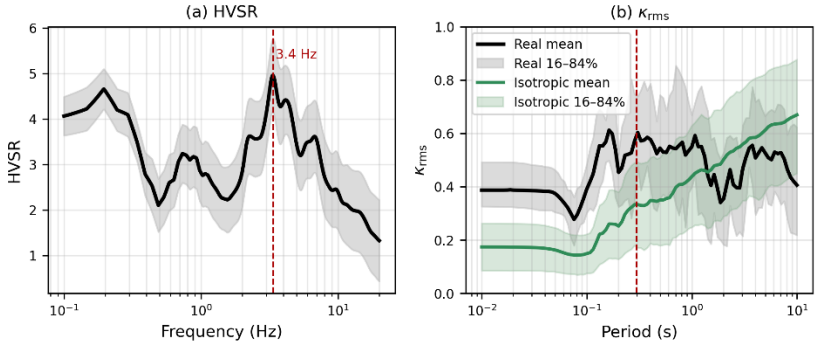

Figure 7. Station ASS. (a) Horizontal-to-vertical spectral ratio (HVSR) showing a pronounced peak near 3.4 Hz. (b) Station-averaged directional anisotropy measure κ_{rms} (black) compared with the isotropic surrogate baseline (green). Shaded bands denote the 16–84% ranges across events. The systematic excess of κ_{rms} relative to the isotropic baseline indicates persistent site-controlled directional amplification.

7. Discussion

Directional variability of horizontal response spectra is commonly interpreted through rotation-based peak measures such as RotD100 and RotD50. In particular, Poulos et al. (2021) showed that the ratio RotD100/RotD50 exhibits systematic dependence on oscillator period and ground-motion duration, and that non-negligible directionality can arise even when the two horizontal components are generated from isotropic stochastic processes. These findings have led to the interpretation that directional variability is primarily a consequence of stochastic peak-factor fluctuations associated with finite-duration random vibration.

The present results suggest a broader interpretation. RotD100/RotD50 is not a direct measure of anisotropy of the directional response field; rather, it reflects the combined influence of two distinct mechanisms: geometric anisotropy of the covariance structure of oscillator response, and stochastic variability associated with peak extraction. As a consequence, the ratio does not isolate the directional structure of the response field itself, but instead mixes covariance-driven anisotropy with the effects of orientation-dependent extrema.

Within the framework developed here, anisotropy emerges already at the level of the root-mean-square response. For finite-duration filtered Gaussian processes, the sample covariance matrix of the two horizontal response components fluctuates according to Wishart statistics, leading to random splitting of its eigenvalues. This produces a realization-dependent elliptical RMS response field, quantified here by κ_{rms}. Directional anisotropy therefore exists prior to peak selection and should not be regarded as a phenomenon generated solely by extreme-value effects.

Peak selection acts on this pre-existing anisotropic field. Because RotD100 is defined from the maximum peak response over orientation, whereas RotD50 represents a median-orientation statistic, the resulting ratio necessarily reflects both covariance anisotropy and peak-factor modulation. From this perspective, the observed dependence of RotD100/RotD50 on oscillator period and duration should not be interpreted exclusively in terms of zero-crossing counts or peak factors. A more fundamental control is the effective number of independent realizations contributing to the covariance estimate of the filtered response, denoted here by N_{eff}. This quantity depends on the correlation structure of the oscillator response and on the energetic duration of the excitation, and it governs the magnitude of the covariance fluctuations that produce directional anisotropy in the first place.

This interpretation has important implications for identifying physical directionality in recorded motions. Even under perfectly isotropic excitation, finite-sample covariance fluctuations generate a stochastic baseline level of directional anisotropy. Physical mechanisms such as rupture directivity, site amplification, or basin effects must therefore be interpreted as perturbations superimposed on a response field that is already anisotropic in a statistical sense. When directionality is assessed only through RotD100/RotD50, these physical contributions may be difficult to distinguish from the combined stochastic variability arising from covariance estimation and peak extraction.

The present framework makes this stochastic baseline explicit: once N_{eff} is specified, the Wishart-derived Beta law provides a compact description of the full stochastic baseline distribution of κ_{rms}^2, which may also be represented in practice by a Kumaraswamy law as a flexible and analytically convenient surrogate.

The framework also clarifies the uncertainty associated with the inferred principal direction. Because this direction is determined from the eigenvectors of the sample covariance matrix, its estimate becomes highly uncertain when N_{eff} is small. The polarization direction inferred from a single record should therefore be interpreted as a realization of a stochastic estimator rather than as a deterministic property of the underlying physical process.

These results also have practical implications. Rotation-based quantities such as RotD50 and RotD100 provide useful summaries of directional response, but they

represent only selected percentiles of spectral ordinates over orientation. By contrast, the κ_{rms}-based formulation characterizes the covariance geometry directly and thereby defines a full stochastic angular field of response spectra. Such a representation offers a more complete basis for applications in which structural orientation may influence seismic demand, including probabilistic seismic hazard analysis, where directional response could in principle be simulated or integrated over orientation rather than approximated through surrogate percentile ratios. However, practical implementation of this framework in seismic hazard analysis will require population-level predictive models for $\kappa_{rms}(T)$, which lie beyond the scope of the present study.

8. Conclusions

This study establishes a stochastic mechanism governing directional spectral anisotropy of earthquake ground motion based on finite-sample covariance statistics of oscillator response. For finite-duration records, fluctuations of the sample covariance matrix of the two horizontal response components produce random polarization governed by Wishart statistics. The magnitude of this anisotropy is controlled primarily by the effective number of statistically independent realizations contributing to the covariance estimate.

To describe this effect, the study introduced the geometric anisotropy measure κ_{rms}, defined from the eigenvalue contrast of the response covariance matrix. Under isotropic Gaussian excitation, κ_{rms}^2 follows the Beta distribution implied by Wishart theory, with the governing effective degrees of freedom determined by oscillator bandwidth and energetic duration. For lightly damped SDOF response, increasing period reduces effective bandwidth and therefore increases anisotropy. Monte Carlo simulations confirm the validity of this framework across stationary filtered Gaussian excitation, non-stationary enveloped excitation, and record-conditioned isotropic surrogates derived from real strong-motion records.

The results further show that directional variability originates in the covariance structure of the RMS response field, while peak-selection operators provide an additional stochastic modulation. Consequently, rotation-based measures such as RotD100 and RotD50, and particularly their ratio, should be interpreted as compound quantities rather than as direct measures of directional anisotropy.

These findings establish a stochastic baseline against which physical directional effects, including rupture directivity, basin response, and directional site amplification, may be interpreted. The proposed κ_{rms}-based formulation therefore provides a more direct description of directional response spectra and a basis for future predictive models of $\kappa_{rms}(T)$. The present work has focused on establishing the stochastic mechanism underlying directional anisotropy and on defining κ_{rms} as its fundamental descriptor; development of population-level predictive models suitable for seismic hazard applications is the subject of ongoing work.

Data availability:

All ground motion data used in this study are available at the European Strong Motion Database (https://esm-db.eu/#/home)

Author contributions:

RR: conceptual framework, mathematical modelling, analysis, coding, drafting and editing VMHA: data collection, processing, coding, drafting, and editing

Appendix A: Derivation of κ_{rms} and Effective Degrees of Freedom

This appendix derives the distribution of the geometric anisotropy measure κ_{rms} under isotropic Gaussian excitation, establishes its exact mean and variance, and extends the result to filtered and non-stationary ground motion through effective degrees of freedom.

A.1 Exact Distribution of κ_{rms} for Independent Gaussian Samples

Let $\hat{\mathbf{C}}$ denote the sample covariance matrix obtained from Nindependent realizations of a two-component zero-mean Gaussian vector process with isotropic population covariance

$$\Sigma = \sigma^2\mathbf{I}.$$

The scaled sample covariance matrix follows a Wishart distribution,

$$N\hat{\mathbf{C}} \sim \mathcal{W}_2(N, \mathbf{I}).$$

Let $\lambda_1 \geq \lambda_2 > 0$denote the eigenvalues of $\hat{\mathbf{C}}$. For the 2×2 isotropic Wishart case, the joint probability density of the ordered eigenvalues is (Muirhead, 2009)

$$f(\lambda_1, \lambda_2) \propto (\lambda_1\lambda_2)^{\frac{N-3}{2}}(\lambda_1 - \lambda_2)\exp\left(-\frac{N}{2}(\lambda_1 + \lambda_2)\right),$$

Define the trace and eigenvalue contrast

$$s = \lambda_1 + \lambda_2, \qquad d = \lambda_1 - \lambda_2.$$

The eigenvalues may then be written

$$\lambda_1 = \frac{s+d}{2}, \lambda_2 = \frac{s-d}{2},$$

with domain

$$s > 0, \qquad 0 \leq d \leq s.$$

The Jacobian of the transformation is

$$\left|\frac{\partial(\lambda_1, \lambda_2)}{\partial(s, d)}\right| = \frac{1}{2}.$$

Substituting these expressions into the joint density gives

$$\mathrm{f(s,d)} \propto \left(\frac{s^2-d^2}{4}\right)^{\frac{N-3}{2}} \mathrm{d}\exp\left(-\frac{N}{2}s\right).$$

The geometric anisotropy measure introduced in the main text is

$$\kappa = \frac{\lambda_1-\lambda_2}{\lambda_1+\lambda_2} = \frac{d}{s}$$

Thus

$$d = s\kappa, 0 \le \kappa \le 1.$$

Substituting $d = s\kappa$ into the density yields

$$\mathrm{f(s,\kappa)} \propto s^{N-1}\kappa(1-\kappa^2)^{\frac{N-3}{2}}\exp\left(-\frac{N}{2}s\right).$$

The Jacobian of the transformation from (s, d) to $(s, \kappa)$is

$$\left|\frac{\partial(s,d)}{\partial(s,\kappa)}\right| = s.$$

After incorporating this factor, the joint density becomes

$$f(s,\kappa) \propto s^{N-1}\exp\left(-\frac{N}{2}s\right)\ \kappa(1-\kappa^2)^{\frac{N-3}{2}}.$$

The trace variable $s$and the anisotropy variable κ are separable in the joint density. Integrating over s therefore yields the marginal distribution of κ:

$$f(\kappa) \propto \kappa(1-\kappa^2)^{\frac{N-3}{2}}, 0 \le \kappa \le 1.$$

Define $y = \kappa^2$. Since

$$\kappa = \sqrt{y}, \frac{d\kappa}{dy} = \frac{1}{2\sqrt{y}},$$

the density of y becomes

$$f(y) \propto (1-y)^{\frac{N-3}{2}}, 0 \le y \le 1.$$

Recognizing the Beta distribution kernel gives

$$\kappa^2 \sim \mathrm{Beta}\left(1, \frac{N-1}{2}\right).$$

A.2 Exact Mean and Variance

Let $b = \frac{N-1}{2}$. From the Beta distribution of κ^2, we obtain

$$\mathbb{E}[\kappa^2] = \frac{1}{1+b} = \frac{2}{N+1}.$$

The exact mean of κ is

$$\mathbb{E}[\kappa] = b\,B\left(\frac{3}{2}, b\right) = \frac{(N-1)\sqrt{\pi}}{4}\frac{\Gamma\left(\frac{N-1}{2}\right)}{\Gamma\left(\frac{N}{2}+1\right)},$$

where $B(\cdot,\cdot)$and $\Gamma(\cdot)$denote the Beta and Gamma functions. The variance follows from

$$\mathrm{Var}(\kappa) = \mathbb{E}[\kappa^2] - (\mathbb{E}[\kappa])^2.$$

These expressions are exact for independent Gaussian samples.

A.3 Large-N Asymptotics

For large N, Stirling approximations (Abramowitz and Stegun, 2006) yield

$$\mathbb{E}[\kappa] \approx \sqrt{\frac{\pi}{2N}}, \mathrm{Var}(\kappa) \approx \frac{4-\pi}{2N}, \mathrm{sd}(\kappa) \approx \sqrt{\frac{4-\pi}{2N}}.$$

Since $\kappa^2 \sim \mathrm{Beta}(1,(N-1)/2)$, the distribution concentrates near zero as $N \to \infty$. Writing $y = \kappa^2$, the Beta density satisfies

$$f_y(y) \propto (1-y)^{(N-3)/2} \approx e^{-Ny/2},$$

for small y. Hence $N\kappa^2$converges to an exponential distribution with mean 2, and therefore $\sqrt{N}\,\kappa$ converges to a Rayleigh distribution with unit scale.

A.4 Effective Degrees of Freedom for Correlated Processes

For continuous time series, successive samples are correlated and the effective number of independent realizations is smaller than the total sample count. Let $X(t)$and $Y(t)$be independent, zero-mean, stationary Gaussian processes with common variance $\sigma^2$and normalized autocorrelation $\rho(\tau)$. Define the sample cross-covariance estimator over duration D:

$$\hat{C}_{XY} = \frac{1}{D}\int_0^D X(t)Y(t)\,dt.$$

Using Isserlis' theorem for fourth-order moments,

$$\mathrm{Var}(\hat{C}_{XY}) = \frac{\sigma^4}{D^2}\int_0^D\int_0^D \rho^2\,(t-s)\,dt\,ds.$$

For D large relative to the correlation decay scale,

$$\mathrm{Var}(\hat{C}_{XY}) \approx \frac{\sigma^4}{D}\int_{-\infty}^{\infty}\rho^2\,(\tau)\,d\tau = \frac{\sigma^4}{D}\,2\int_0^{\infty}\rho^2\,(\tau)\,d\tau.$$

Matching this to the Wishart variance $\sigma^4/N_{\mathrm{eff}}$ defines

$N_{\mathrm{eff}} \approx \frac{D}{2\int_0^{\infty}\rho^2(\tau)\,d\tau}$Thus, effective degrees of freedom are governed by the integral of squared autocorrelation rather than by zero-crossing rates.

A.5 Evaluation for Lightly Damped SDOF Response

For narrowband SDOF pseudo-acceleration response with damping ratio $\xi$and natural frequency ω_n, the normalized autocorrelation is approximated by

$$\rho(\tau) = e^{-\alpha|\tau|}\cos(\omega_d\tau), \alpha = \xi\omega_n.$$

Carrying out the integration yields

$$\int_0^\infty \rho^2(\tau)\, d\tau = \frac{1}{8\alpha} + \frac{\alpha}{4(\alpha^2+\omega_d^2)}.$$

For light damping $\omega_d \gg \alpha$, the second term is negligible, giving

$$\int_0^\infty \rho^2(\tau)\, d\tau \approx \frac{1}{4\alpha}.$$

Substituting into the definition of N_{eff},

$$N_{\text{eff}} \approx 2\alpha D = 2\xi\omega_n D = \frac{4\pi\xi D}{T}.$$

This establishes the fundamental period scaling of effective degrees of freedom.

A.6 Non-stationary Excitation and Energetic Effective Duration

Consider amplitude-modulated excitation

$$g_i(t) = w(t)u_i(t), i = 1,2,$$

where $u_i(t)$ are stationary Gaussian processes and $w(t)$ is a deterministic envelope varying slowly relative to the correlation time of $u_i(t)$.

Following the same variance-matching procedure as above,

$$N_{\text{eff}} = \frac{\left(\int w^2(t)\, dt\right)^2}{\int w^4(t)\, dt} \cdot \frac{1}{2\int_0^\infty \rho_u^2(\tau)\, d\tau}.$$

Define the energetic effective duration

$$D_{\text{eff}}^{(g)} = \frac{\left(\int w^2(t)\, dt\right)^2}{\int w^4(t)\, dt}.$$

Then

$$N_{\text{eff}}(T) \approx \frac{4\pi\xi D_{\text{eff}}^{(g)}}{T}.$$

Thus, envelope non-stationarity modifies anisotropy scaling solely through reduction of effective duration.

A.7 Unified Expression

Combining Sections A.1–A.6:

The exact baseline distribution of geometric anisotropy is

$$\kappa_{\text{rms}}^2 \sim \text{Beta}\left(1, \frac{N_{\text{eff}}(T)-1}{2}\right).$$

For lightly damped SDOF response under envelope modulation,

$$N_{\mathrm{eff}}(T) \approx \frac{4\pi\xi D_{\mathrm{eff}}^{(g)}}{T}.$$

The large-N_{eff} asymptotic mean and standard deviation are

$$\mathbb{E}[\kappa_{\mathrm{rms}}(T)] \approx \sqrt{\frac{T}{8\xi D_{\mathrm{eff}}^{(g)}}}, \mathrm{sd}(\kappa_{\mathrm{rms}}(T)) \approx \sqrt{\frac{4-\pi}{8\pi\xi D_{\mathrm{eff}}^{(g)}}}\sqrt{T}.$$

These results formalize the stochastic baseline governing directional anisotropy and clarify how oscillator period, damping, and energetic duration jointly control both the mean and dispersion of κ_{rms}.

References

Abramowitz, M., Stegun, I.A., 2006. Handbook of mathematical functions: with formulas, graphs, and mathematical tables. National Bureau of Standards Washington, DC.

Boore, D.M., 2010. Orientation-Independent, Nongeometric-Mean Measures of Seismic Intensity from Two Horizontal Components of Motion. Bull. Seismol. Soc. Am. 100, 1830–1835. https://doi.org/10.1785/0120090400

Boore, D.M., Kishida, T., 2017. Relations between some horizontal-component ground-motion intensity measures used in practice. Bull. Seismol. Soc. Am. 107, 334–343.

Bradley, B.A., Baker, J.W., 2015. Ground motion directionality in the 2010–2011 Canterbury earthquakes. Earthq. Eng. Struct. Dyn. 44, 371–384. https://doi.org/10.1002/eqe.2474

Burjánek, J., Edwards, B., Fäh, D., 2014. Empirical evidence of local seismic effects at sites with pronounced topography: a systematic approach. Geophys. J. Int. 197, 608–619. https://doi.org/10.1093/gji/ggu014

Campbell, K.W., 1991. An empirical analysis of peak horizontal acceleration for the Loma Prieta, California, earthquake of 18 October 1989. Bull. Seismol. Soc. Am. 81, 1838–1858. https://doi.org/10.1785/BSSA0810051838

Kotha, S.R., Cotton, F., Bindi, D., 2019. Empirical Models of Shear-Wave Radiation Pattern Derived from Large Datasets of Ground-Shaking Observations. Sci. Rep. 9, 981. https://doi.org/10.1038/s41598-018-37524-4

Kumaraswamy, P., 1980. A generalized probability density function for double-bounded random processes. J. Hydrol. 46, 79–88. https://doi.org/https://doi.org/10.1016/0022-1694(80)90036-0

Lanzano, G., Luzi, L., Cauzzi, C., Bienkowski, J., Bindi, D., Clinton, J., Cocco, M., D'Amico, M., Douglas, J., Faenza, L., Felicetta, C., Gallovic, F., Giardini, D., Ktenidou, O., Lauciani, V., Manakou, M., Marmureanu, A., Maufroy, E., Michelini, A., Özener, H., Puglia, R., Rupakhety, R., Russo, E., Shahvar, M., Sleeman, R., Theodoulidis, N., 2021. Accessing European Strong-Motion Data: An Update on ORFEUS Coordinated Services. Seismol. Res. Lett. 92, 1642–1658. https://doi.org/10.1785/0220200398

Muirhead, R.J., 2009. Aspects of multivariate statistical theory, Wiley series in probability and statistics. Wiley.

Pischiutta, M., Salvini, F., Fletcher, J., Rovelli, A., Ben-Zion, Y., 2012. Horizontal Polarization of Ground Motion in the Hayward Fault Zone at Fremont, California:

Dominant Fault-High-Angle Polarization and Fault-Induced Cracks. Geophys. J. Int. 188, 1255–1272. https://doi.org/10.1111/j.1365-246X.2011.05319.x

Poulos, A., Miranda, E., Baker, J.W., 2021. Evaluation of Earthquake Response Spectra Directionality Using Stochastic Simulations. Bull. Seismol. Soc. Am. 112, 307–315. https://doi.org/10.1785/0120210101

Rupakhety, R., Hernández-Aguirre, V.M., 2026a. Rotation-Invariant Ground-Motion as Directional Selection Operators: A Closed-Form Framework for RotD Response Spectra. https://doi.org/10.31223/X50R1C

Rupakhety, R., Hernández-Aguirre, V.M., 2026b. Directional Peak Factors of Strong-Motion Response Spectra: A Stochastic Field Representation on the Circle. https://doi.org/10.31223/X5VX74

Rupakhety, R., Sigbjörnsson, R., 2013. Rotation-Invariant Measures of Earthquake Response Spectra. Bull. Earthq. Eng. 11, 1885–1893. https://doi.org/10.1007/s10518-013-9472-1

Rupakhety, R., Sigurdsson, S.U., Papageorgiou, A.S., Sigbjörnsson, R., 2011. Quantification of ground-motion parameters and response spectra in the near-fault region. Bull. Earthq. Eng. 9, 893–930. https://doi.org/10.1007/s10518-011-9255-5

Shahi, S.K., Baker, J.W., 2014. NGA-West2 Models for Ground Motion Directionality. Earthq. Spectra 30, 1285–1300. https://doi.org/10.1193/040913EQS097M

Vidale, J.E., Bonamassa, O., Houston, H., 1991. Directional site resonances observed from the 1 october 1987 whittier narrows, california, earthquake and the 4 october aftershock. Earthq. Spectra 7, 107–125. https://doi.org/10.1193/1.1585616

Watson-Lamprey, J.A., Boore, D.M., 2007. Beyond Sa GMRotI: Conversion to Sa Arb, Sa SN, and Sa MaxRot. Bull. Seismol. Soc. Am. 97, 1511–1524.

Wishart, J., 1928. The generalised product moment distribution in samples from a normal multivariate population. Biometrika 20A, 32–52. https://doi.org/10.1093/biomet/20A.1-2.32